

Searching for Anomalous Microwave Emission in nearby galaxies

K-band observations with the Sardinia Radio Telescope

S. Bianchi¹, M. Murgia², A. Melis², V. Casasola³, F. Galliano⁴, F. Govoni², A. P. Jones⁵, S. C. Madden⁴,
R. Paladino³, F. Salvestrini¹, E. M. Xilouris⁶, and N. Ysard⁵

¹ INAF-Osservatorio Astrofisico di Arcetri, L. E. Fermi 50, 50125, Firenze, Italy

e-mail: simone.bianchi@inaf.it

² INAF-Osservatorio Astronomico di Cagliari, Via della Scienza 5, 09047 Selargius (CA), Italy

³ INAF-Istituto di Radioastronomia-Via P. Gobetti, 101, 40129 Bologna, Italy

⁴ AIM, CEA, CNRS, Université Paris-Saclay, Université Paris Diderot, Sorbonne Paris Cité, 91191 Gif-sur-Yvette, France

⁵ Université Paris-Saclay, CNRS, Institut d'Astrophysique Spatiale, 91405 Orsay, France

⁶ National Observatory of Athens, Institute for Astronomy, Astrophysics, Space Applications and Remote Sensing, Ioannou Metaxa and Vasileos Pavlou, 15236 Athens, Greece

ABSTRACT

Aims. We observed four nearby spiral galaxies (NGC 3627, NGC 4254, NGC 4736 and NGC 5055) in the K band with the 64-m Sardinia Radio Telescope, with the aim of detecting the Anomalous Microwave Emission (AME), a radiation component presumably due to spinning dust grains, observed so far in the Milky Way and in a handful of other galaxies only (most notably, M 31).

Methods. We mapped the galaxies at 18.6 and 24.6 GHz and studied their global photometry together with other radio-continuum data from the literature, in order to find AME as emission in excess of the synchrotron and thermal components.

Results. We only find upper limits for AME. These non-detections, and other upper limits in the literature, are nevertheless consistent with the average AME emissivity from the few detections: it is $\epsilon_{30\text{ GHz}}^{\text{AME}} = 2.4 \pm 0.4 \times 10^{-2} \text{ MJy sr}^{-1} (M_{\odot} \text{ pc}^{-2})^{-1}$ in units of dust surface density (equivalently, $1.4 \pm 0.2 \times 10^{-18} \text{ Jy sr}^{-1} (\text{H cm}^{-2})^{-1}$ in units of H column density). We finally suggest to search for AME in quiescent spirals with relatively low radio luminosity, such as M 31.

Key words. radio continuum: galaxies – galaxies: ISM – galaxies: photometry – dust, extinction

1. Introduction

Observations in the Milky Way (MW) at $10 \lesssim \nu/\text{GHz} \lesssim 50$ have revealed emission in excess of the well known thermal dust, free-free and synchrotron radiation components: it is the Anomalous Microwave Emission (AME), peaking at $\nu \approx 30$ GHz and correlating with thermal dust emission at higher frequencies (for a review, see Dickinson et al. 2018). AME is seen both in the diffuse medium (Planck Collaboration XXV 2016, hereafter PLA16) as well as on isolated clouds, where its characteristics are reported to vary with environment (Planck Collaboration Int. XV 2014).

The most popular explanation for AME involves electric dipole emission from spinning dust grains (Draine & Lazarian 1998a; Ali-Haïmoud et al. 2009). These grains must be small ($\lesssim 10^{-9}$ m) in order to spin fast and emit at ≈ 30 GHz: both PAHs (Draine & Lazarian 1998b) or nanosilicate (Hoang et al. 2016) have been proposed. Alternative explanations have AME produced by microwave enhancements in the dust emission cross section, due to magnetic inclusions in grains (Draine & Lazarian 1999) or to their amorphous structure (Jones 2009; Nashimoto et al. 2020). Yet, there is no definitive evidence for the effective emission mechanism: some works support the spinning-dust hypothesis (Ysard et al. 2010; Harper et al. 2015; Bell et al. 2019) while others find a fainter correlation of AME with PAH emission (Hensley et al. 2016).

Beyond the MW AME has been observed only in a handful of galaxies. It has been seen in a single star-forming region in

NGC 6946 (Murphy et al. 2010) and in a compact radio source in NGC 4725 (Murphy et al. 2018). So far, the most convincing case for the detection of AME in the global Spectral Energy Distribution (SED) of a galaxy is that of M 31, the Andromeda galaxy. Planck Collaboration Int. XXV (2015) found that AME contributes to $\approx 35\%$ of the flux density at 30 GHz, though this was a marginal detection. Battistelli et al. (2019) claimed a stronger detection and an AME contribution of 75%; they obtained it after constraining the synchrotron and thermal components at lower frequency (6.6 GHz; see also Fatigoni et al. 2021), using observations from the 64-m Sardinia Radio Telescope (SRT; Prandoni et al. 2017). Much less prominent is AME in the Large and Small Magellanic Clouds (LMC and SMC, respectively), where it is found to contribute to $\approx 10\%$ of the SED at 22.8 GHz (PLA16). In these objects (but also in M 31) a careful subtraction of the contribution from the Cosmic Microwave Background (CMB) is needed. In fact, analysis based on previous CMB templates claimed no detection for the LMC, and a stronger AME component for the SMC (Planck Collaboration XVII 2011). The search for AME in other galaxies proved unsuccessful (Peel et al. 2011, hereafter P11; Tibbs et al. 2018; other unpublished non-detections are also reported by Dickinson et al. 2018).

In this paper, we report on our attempt at detecting AME in four nearby spiral galaxies, using SRT K-band (18 - 26.5 GHz) observations. The sample, observations and image processing are described in Sect. 2; photometry and SED fitting are pre-

Table 1. Observing log.

Date	Band GHz	τ	Target	N. of maps along RA+Dec
03/01/21	24.6	0.18	NGC 3627	11+11
04/01/21	18.6	0.05	NGC 4254	7+7
05/01/21	18.6	0.05	NGC 3627	7+6
02/02/21	24.6	0.25	NGC 4254	12+10
05/02/21	24.6	0.16	NGC 3627	9+9
			NGC 4254	4+3
22/03/21	24.6	0.19	NGC 4736	7+6
			NGC 5055	7+7
31/03/21	18.6	0.08	NGC 3627	1+1
			NGC 4736	7+7
			NGC 5055	7+7
03/04/21	24.6	0.30	NGC 5055	6+6

sented in Sect. 3; the upper limits we find for AME are discussed together with other observations in the literature in Sect. 4; in Sect. 5 we draw our conclusions.

2. Sample, observations and data reduction

Our sample consists of four nearby spirals: NGC 3627 (M 66), NGC 4254 (M 99), NGC 4736 (M 94) and NGC 5055 (M 63). The objects were chosen for a pilot project to extend the SED knowledge to the poorly known 15-300 GHz frequency range (Bianchi et al. 2021). In fact, an excellent coverage is available in the UV-to-submm (from the DustPedia database; Davies et al. 2017) and in the mid radio-continuum (Tabatabaei et al. 2017, hereafter, T17); furthermore, the galaxies are among the targets currently being mapped at millimeter wavelengths with the IRAM 30-m telescope and NIKA2 camera, within the IMEGIN program (Katsioli et al. 2021; Ejlali et al. 2021).

Observations at SRT were carried out during program 43-20 (January 2021) and related DDT programs 1-21 (February 2021) and 7-21 (March-April 2021). We used the K-band 7-feed spectro-polarimetric receiver (Orfei et al. 2010), coupled with the Sardinia Roach2-based Digital Architecture for Radio Astronomy back end (SARDARA; Melis et al. 2018). We observed two 1.2 GHz bands centered at 18.6 and 24.6 GHz (HPBW = 57'' and 45'', respectively). The bands were covered by 1.46 MHz frequency channels in full Stokes mode. Observations were done with an on-the-fly scheme over an area of 16' \times 16', centered on each galaxy. In order to remove scan noise efficiently, several maps were taken along orthogonal RA and Dec directions, with scan speed 2'/s and scan separation HPBW/3 (each map lasting about 20 minutes). The observing log is given in Table 1.

The spectral cubes were reduced using the proprietary Single-dish Spectral-polarimetry Software (SCUBE; Murgia et al. 2016). Here we only describe the procedure used for total-intensity data, as no polarization was detected. The flux density was brought to the scale of Perley & Butler (2017) using the calibrators 3C 147 and 3C 286. The two sources were used also as band pass calibrators. We corrected the data to compensate for the atmosphere opacity that was derived by mean of sky dips performed during each observing session. We modeled the observed T_{sys} trends with the airmass model to obtain the zenithal opacity, τ (see Table 1). We evaluated the consistency of the calibration by cross-checking the flux density of 3C 147 against that of 3C 286. Using 3C 147 as primary calibrator, and considering measurements in different weather conditions, we found that on average the observed 3C 286 flux density is about $\pm 10\%$ the ex-

Table 2. Aperture definition and SRT photometry.

	Apertures		$S_{18.6 \text{ GHz}}$ mJy	$S_{24.6 \text{ GHz}}$ mJy
	Size	P.A.		
NGC 3627	6' \times 6'	0°	71 \pm 14	87 \pm 13
NGC 4254	6' \times 6'	0°	64 \pm 15	42 \pm 19
NGC 4736	6' \times 6'	0°	61 \pm 7	71 \pm 15
NGC 5055	10.2' \times 5.5'	103°	67 \pm 10	79 \pm 9

pected value at both 18.6 and 24.6 GHz. We assume the dispersion of the reproducibility of 3C 286 flux density as an estimate of the systematic uncertainties in our calibration procedure due to errors in pointing, opacity correction, atmospheric fluctuations removal, etc. This systematic error is consistent with what found by Loi et al. (2020) using a much larger data set.

We removed the baseline scan-by-scan by fitting a 2nd order polynomial to the "cold-sky" regions around each target. We masked the target and removed all the surrounding point sources (from the 1.4 GHz catalog by Condon et al. 1998). In this way, we removed the contributions from the receiver noise, the atmospheric emission, and the large-scale foreground sky emission and we retained the target emission only, on scales smaller than the mask size. We then stack the data from all feeds to reduce the noise level. We combined the RA and Dec scans by mixing their stationary wavelet transform (SWT) coefficients (see Murgia et al. 2016). The SWT stacking, conceptually similar to the weighted Fourier merging (Emerson & Graeve 1988), is very effective in isolating and removing the noise oriented along the scan direction. Finally, we average all spectral channels to increase the signal-to-noise ratio and produce maps with scale 15''/pixel.

3. Results

The total intensity maps of the four targets at 18.6 and 24.6 GHz are shown in Fig. 1. In all cases we detected diffuse emission, resembling the aspect, despite the lower resolution, observed in the far-infrared/submillimeter (FIR-submm) or in the radio (see Sect. A.1 and Fig. A.1). In particular, the emission in NGC 3627 peaks at both ends where the central bar meets the spiral arms, and parts of the ring of NGC 4736 are visible in the 24.6 GHz image.

In Fig. 1 we also show the sky apertures used to derive the total flux density S_{ν} . Due to the small size of our maps, the apertures are taken to be small but sufficiently wide to enclose all the emission that is deemed to come from the galaxies, in both the 18.6 and 24.6 GHz maps. The same apertures were placed on a few positions outside of the targets to estimate the residual background and its fluctuations (see, e.g., Auld et al. 2013; Clark et al. 2018). This procedure gave results consistent with the more traditional sky estimate from an annulus around the source. In Table 2 we give S_{ν} and its uncertainty, to which we added, in quadrature, the systematic error discussed in Sect. 2.

In Fig. 2 we show the SEDs of the four galaxies in the 1-30 GHz range, using the SRT photometry and the mid-radio continuum data from T17. Ideally, one should use flux densities obtained by integrating maps over the same aperture at all frequencies. Instead, the flux densities in the compilation of T17 refer to apertures based on the optical size of each galaxy, which are larger than what we used above. Nevertheless, we find that our choice does not alter significantly the estimate of the flux density at SRT frequencies (tests are described in Sect. A.1). We model the SED as the sum of three continuum components: i)

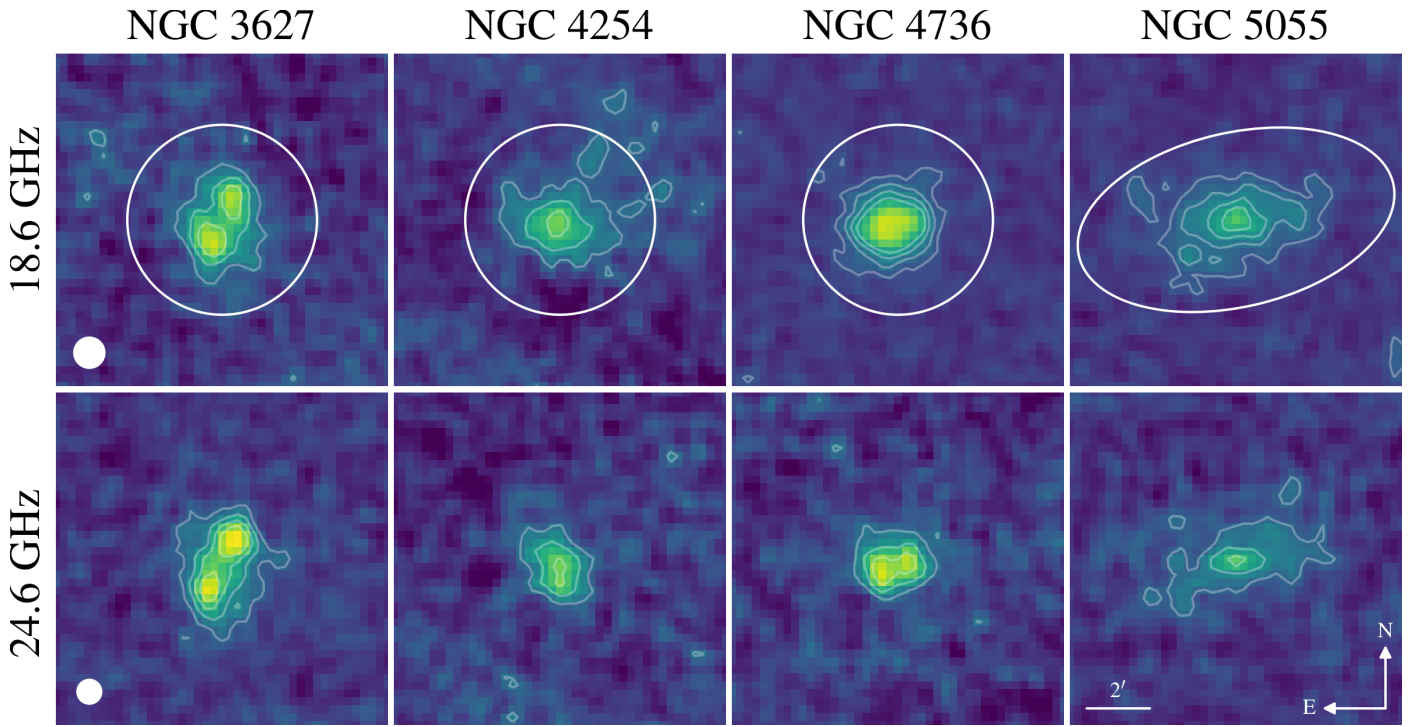


Fig. 1. Total intensity maps with contours at 3, 6, 9 and 12 \times the sky $r.m.s.$. At 18.6 GHz, $r.m.s.$ = 1.2, 1.1, 0.6, 0.7 mJy beam $^{-1}$, for NGC 3627, NGC 4254, NGC 4736, NGC 5055, respectively; at 24.6 GHz, $r.m.s.$ = 0.7, 0.8, 0.9, 0.7 mJy beam $^{-1}$. Photometry apertures and HPBWs are also shown.

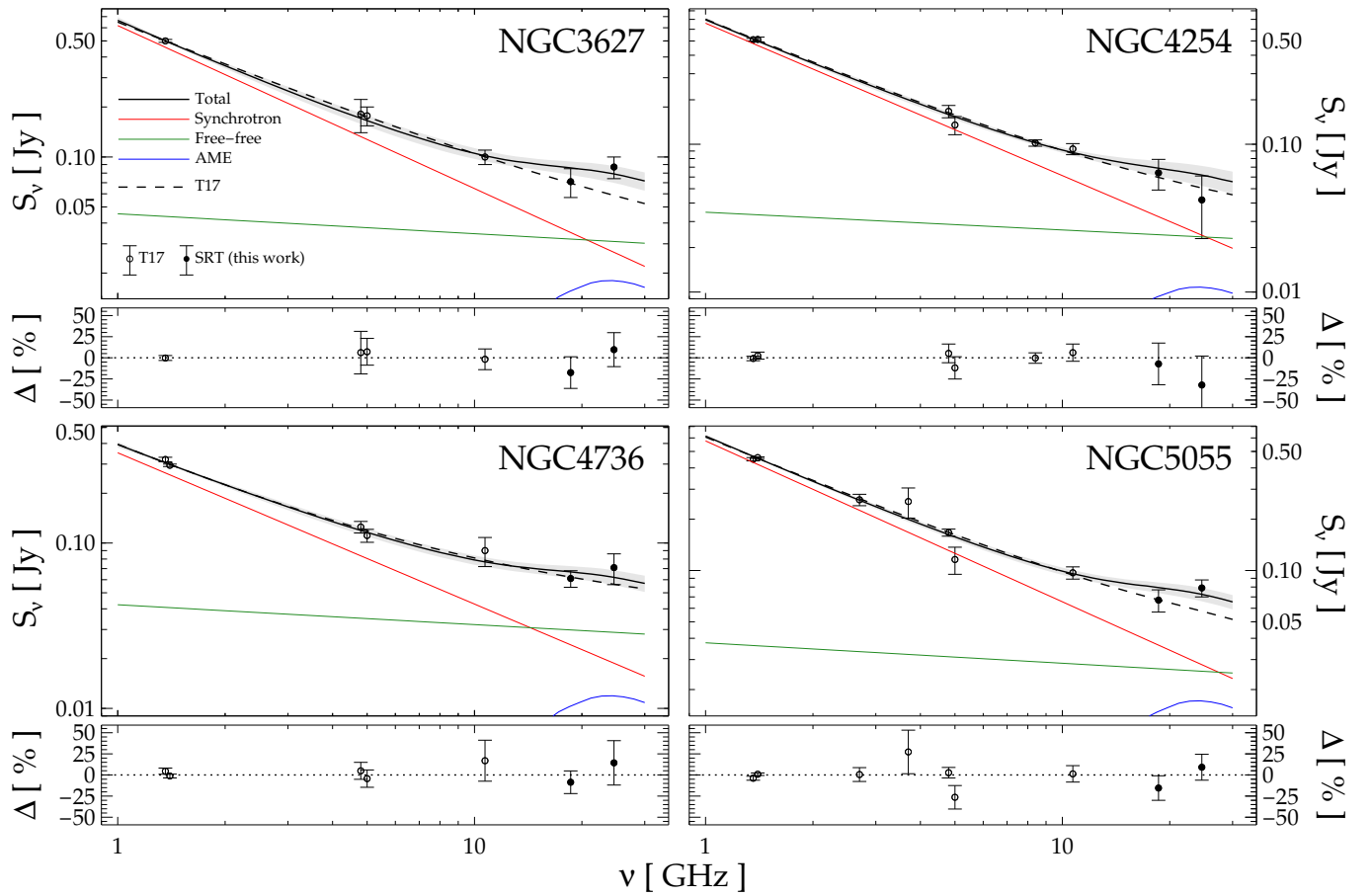


Fig. 2. Global SEDs and fits, with their uncertainty. We also show each SED component and the T17 fit. Under each SED, we show the residuals Δ =data-model (in percentage of the model).

Table 3. Fit parameters, relative contribution of the various components at 5 and 24.6 GHz and upper limits for $S_{24.6 \text{ GHz}}^{\text{AME}}$.

	α	$S_{5 \text{ GHz}}^{\text{sy}}$ mJy	$S_{5 \text{ GHz}}^{\text{ff}}$ mJy	$S_{24.6 \text{ GHz}}^{\text{AME}}$ mJy	$S_{5 \text{ GHz}}^{\text{sy}}$ %	$S_{5 \text{ GHz}}^{\text{ff}}$ %	$S_{24.6 \text{ GHz}}^{\text{sy}}$ %	$S_{24.6 \text{ GHz}}^{\text{ff}}$ %	$S_{24.6 \text{ GHz}}^{\text{AME}}$ %	$S_{24.6 \text{ GHz}}^{\text{AME u.l.}}$ mJy
NGC 3627	$0.98^{+0.20}_{-0.12}$	127^{+30}_{-37}	38^{+29}_{-26}	18^{+16}_{-12}	77	23	35	41	24	< 44
NGC 4254	$1.03^{+0.16}_{-0.09}$	125^{+22}_{-29}	29^{+23}_{-19}	11^{+12}_{-8}	81	19	41	41	18	< 32
NGC 4736	$0.91^{+0.21}_{-0.13}$	81^{+23}_{-25}	35^{+23}_{-22}	12^{+11}_{-8}	70	30	32	48	20	< 30
NGC 5055	$0.94^{+0.12}_{-0.08}$	126^{+21}_{-25}	31^{+23}_{-21}	17^{+12}_{-11}	80	20	40	36	24	< 36

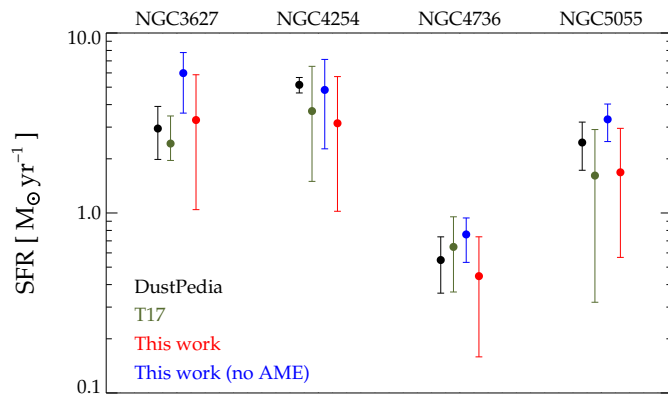
synchrotron radiation, dominating in the upper end of the range, which -in the optically thin regime- can be described by a power-law; ii) free-free, emission, almost flat with frequency, emerging over synchrotron as the frequency increases; iii) AME, expected to contribute at the highest frequencies considered here. It is:

$$S_{\nu} = S_{5 \text{ GHz}}^{\text{sy}} \times \left(\frac{\nu}{5 \text{ GHz}}\right)^{\alpha} + S_{5 \text{ GHz}}^{\text{ff}} \times \left(\frac{\nu}{5 \text{ GHz}}\right)^{-0.12} + S_{\nu}^{\text{AME}}, \quad (1)$$

where α is the synchrotron spectral index, $S_{5 \text{ GHz}}^{\text{sy}}$ and $S_{5 \text{ GHz}}^{\text{ff}}$ are the amplitudes of the synchrotron and free-free component at 5 GHz, respectively, and the weak frequency dependence of the free-free continuum is taken from Draine (2011). For the AME component, we adopted the spectral template of Battistelli et al. (2019), derived by averaging theoretical predictions over a variety of ISM environments, using the `spdust.2` code (Ali-Haïmoud et al. 2009; Silsbee et al. 2011) and neglecting the most extreme cases presented in Fig. 2 of Dickinson et al. (2018). We scale the template on its amplitude at 24.6 GHz, $S_{24.6 \text{ GHz}}^{\text{AME}}$ and, as in Battistelli et al. (2019), we keep its peak fixed (it is located at $\nu \approx 25$ GHz). We do not include thermal emission from dust, negligible in the spectral range we considered (see, e.g., P11).

We fit Eq. 1 to the data using the `emcee` Python implementation (version 3.0) of the Goodman & Weare’s Affine Invariant Markov chain Monte Carlo (MCMC) Ensemble sampler (Foreman-Mackey et al. 2013). We adopted positive flat priors for α , $S_{5 \text{ GHz}}^{\text{sy}}$, $S_{5 \text{ GHz}}^{\text{ff}}$, $S_{24.6 \text{ GHz}}^{\text{AME}}$ and obtained their posterior probability distribution function (PDF) by sampling the likelihood function, conditional on the data. We used 100 walkers, initially distributed around the T17 fit (assuming negligible AME), and run a chain of 2×10^4 steps. The PDFs were obtained after deriving the integrated autocorrelation time and neglecting a few times this number of steps to remove the *burn-in* phase from the chain. We tested on the convergency of the results by varying the initial conditions (setting higher values for AME), the number of walkers and samples. The fits and uncertainties are shown in Fig. 2, while in Table 3 we present the estimate and uncertainty of each parameter, derived from the median and 0.16 and 0.84 percentiles (see Fig. A.2 for the Bayesian corner plots).

The only parameters estimated at high significance are those for the synchrotron component: in particular, our α estimates are consistent within the errors with those of T17. Much more uncertain is the estimate of the free-free component: it is degenerate with that of synchrotron at lower frequencies, contributing to 20-30 % of the continuum flux density at 5 GHz (see Table 3); it is also degenerate with the AME component, as the largest contribution to the SED of both emissions insists on the same spectral window, for $\nu \gtrsim 15$ GHz. Because of this, we expected our estimates to be more uncertain than those in T17, that do not include an AME component and use only data with $\nu \lesssim 10$ GHz. We compare the results from the two fits in Fig. 3, where we have converted $S_{5 \text{ GHz}}^{\text{ff}}$ into the SFR, since the free-free emission is proportional to the amount of free electrons, and thus to the photoionizing rate (Murphy et al. 2011; T17). Despite the larger

**Fig. 3.** Comparison between SFRs from DustPedia and from $S_{5 \text{ GHz}}^{\text{ff}}$ (see text for details).

uncertainties (but not for NGC 5055), our results are still compatible with T17. Both estimates are also broadly consistent with the SFRs derived by DustPedia UV-to-submm SED, thus independently of observations in the radio. As shown by Fig. 3, the advantage of deriving the SFR from the radio thermal radiation, in a spectral range unaffected by dust extinction, is compounded by the larger uncertainties due to the fit degeneracies. Data at frequencies above 25 GHz is needed to solve these degeneracies and obtain more precise determinations of SFR from the radio continuum and of the presence of AME.

All three components contribute to the continuum at 24.6 GHz (see Table 3): the synchrotron and free-free fractions are about the same, $\sim 40\%$, while the AME fraction is about half that value, $\sim 20\%$. However, in no case the fitted $S_{24.6 \text{ GHz}}^{\text{AME}}$ is significant. Thus, in the following discussion we use upper limits for $S_{24.6 \text{ GHz}}^{\text{AME}}$, derived from the 0.95 percentile of the PDF.

Within this work, we also tried to fit the SED without including the AME component in Eq. 1: upper limits on $S_{24.6 \text{ GHz}}^{\text{AME}}$ were then obtained from the residuals between observations and model (as done in P11). In this case we still obtained plausible fits (not shown) by steepening the synchrotron spectrum and raising the free-free contribution: with respect to fits with AME included, $S_{5 \text{ GHz}}^{\text{ff}}$ values are larger by a factor ~ 2 (see the corresponding SFRs in Fig. 3) while the AME upper limits becomes smaller. In fact, as pointed out by P11, this approach might result in a bias towards a lower AME estimate. Nevertheless, either using the $S_{24.6 \text{ GHz}}^{\text{AME}}$ upper limits from the full fit or those from the residuals to a no-AME fit has no consequence for the rest of the discussion in this work.

4. AME emissivity

In the MW, AME has often been studied in correlation with dust emission at $100 \mu\text{m}$ (3 THz) (Dickinson et al. 2018). For

Galactic latitudes $|b| > 10^\circ$, PLA16 find $S_{22.8 \text{ GHz}}^{\text{AME}}/S_{3 \text{ THz}} = 3.4 \pm 0.3 \times 10^{-4}$. Usually, the MW estimate has been compared with observations in other galaxies: while Battistelli et al. (2019) derive in M31 a value for $S_{30 \text{ GHz}}^{\text{AME}}/S_{3 \text{ THz}}$ consistent with the MW, P11 and Tibbs et al. (2018) find smaller ratios for their targets; the same is true for our targets. For simplicity, we use the same notation for the MW (and Magellanic Clouds), where the ratio is derived by correlating surface brightness maps, and the rest of the galaxies we discuss, where it is a ratio between flux densities (equivalent to a ratio between galaxy-averaged surface brightnesses). Also, the ratios are obtained at different frequencies: nevertheless they are not expected to change much in the 20-30 GHz range (by $\lesssim 10\%$ for the template of Battistelli et al. 2019). Thus, we neglect any frequency dependence and use for all objects the term $S_{30 \text{ GHz}}^{\text{AME}}/S_{3 \text{ THz}}$, also when referring to the SRT 24.6 GHz estimates (see Table A.1).

Tibbs et al. (2012) questioned the validity of $S_{30 \text{ GHz}}^{\text{AME}}/S_{3 \text{ THz}}$ as an indicator of the AME emissivity: in fact, the $100 \mu\text{m}$ flux density - near the peak of dust emission - depends strongly on the grain temperature; instead, under the spinning-grain hypothesis, the low intensity radiation fields responsible for diffuse dust emission have little influence on AME, at least for low density environments (Ali-Haïmoud et al. 2009; Ysard et al. 2011). A better characterization for AME is to derive its emissivity, i.e. its surface brightness J_{ν}^{AME} normalized to a tracer of the amount of underlying emitting material. Under the assumption that AME is due to dust, we can write

$$\epsilon_{30 \text{ GHz}}^{\text{AME}} = \frac{J_{30 \text{ GHz}}^{\text{AME}}}{\Sigma_d} = \frac{S_{30 \text{ GHz}}^{\text{AME}}}{S_{3 \text{ THz}}} \kappa_{3 \text{ THz}}^d B_{3 \text{ THz}}(T_d), \quad (2)$$

where Σ_d is the dust mass surface density, $B_{3 \text{ THz}}(T_d)$ the Planck function for the dust temperature T_d and $\kappa_{3 \text{ THz}}^d$ the dust absorption cross-section¹. For our targets, temperatures (and dust masses) were obtained from single-temperature modified blackbody (MBB) fits to FIR/sum SEDs by Nersesian et al. (2019), after assuming the average properties of MW diffuse dust from The Heterogeneous dust Evolution Model for Interstellar Solids (THEMIS; Jones et al. 2017): in particular, THEMIS dust is characterized by an effective absorption cross section that can be described by $\kappa_{\nu}^d / (\text{pc}^2/\text{M}_{\odot}) = 6.9 \times 10^{-3} \times (\nu/3 \text{ THz})^{1.79}$ (Galiano et al. 2018).

The emissivity $\epsilon_{30 \text{ GHz}}^{\text{AME}}$ is shown as a function of T_d in Fig. 4, where we also included the estimates for the MW and M 31, those for the LMC and SMC (PLA16); and the upper limits for M 33 (Tibbs et al. 2018) and NGC 253, NGC 3034 and NGC 4945 (P11). Seeking for uniformity in the estimate of dust parameters we performed MBB/THEMIS fits also for these objects (Table A.1). Almost all the upper limits are compatible with the estimates in the MW and M 31 and also the LMC and SMC values are not far off. Only for M 33 $\epsilon_{30 \text{ GHz}}^{\text{AME}}$ is much lower, suggesting different properties of the interstellar medium (ISM) and/or the dust grains for this galaxy with respect to the MW and M 31. After computing the spinning-grain emission for the THEMIS dust distribution, most of the spread in Fig. 4 can be reconciled with variations in the ISM density and radiation field intensity (Ysard et al. in preparation).

¹ Equivalently, Eq. 2 can be written as

$$\epsilon_{30 \text{ GHz}}^{\text{AME}} = \frac{S_{30 \text{ GHz}}^{\text{AME}}}{M_d/D^2}, \quad (3)$$

where M_d is the galaxy's dust mass and D is the distance used for its determination (Eq. 3, as Eq. 2, being eventually independent on D ; see also Bianchi et al. 2019).

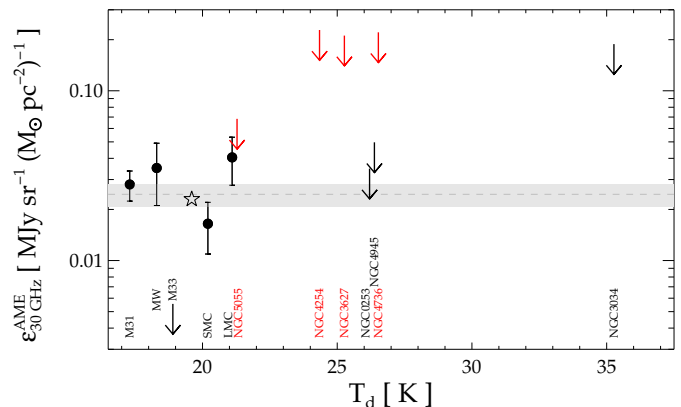


Fig. 4. $\epsilon_{30 \text{ GHz}}^{\text{AME}}$ vs T_d . Red symbols are for SRT targets. The shaded area shows the weighted average and standard deviation of $\epsilon_{30 \text{ GHz}}^{\text{AME}}$; the star is the PLA16 estimate for the MW (see text for details).

The weighted average of the four determinations is $\epsilon_{30 \text{ GHz}}^{\text{AME}} = 2.4 \pm 0.4 \times 10^{-2} \text{ MJy sr}^{-1} (\text{M}_{\odot} \text{ pc}^{-2})^{-1}$ (shaded area in Fig. 4). For the dust-to-gas mass ratio of the THEMIS model (0.0074), this converts to $1.4 \pm 0.2 \times 10^{-18} \text{ Jy sr}^{-1} (\text{H cm}^{-2})^{-1}$ (in units of H column density). A possible caveat here can be due to the uncertainties inherent to the determination of the dust column density and to the necessity of using coherent methods for all the objects. For example, if we convert the average emissivity to units of surface brightness per dust optical depth at $850 \mu\text{m}$ (it is $S_{30 \text{ GHz}}^{\text{AME}}/\tau_{850 \mu\text{m}}^d = \epsilon_{30 \text{ GHz}}^{\text{AME}}/\kappa_{353 \text{ GHz}}^d$) and express it in temperature (at 22.8 GHz) we obtain $10 \pm 2 \text{ K}$, a value close to what PLA16 derive - but for the MW only. The difference might reside in the different reference frequency for estimating the dust surface density, and in the derivation of the dust temperature from the observed SED (using a fixed dust model, in our case, vs a fit of the opacity cross section dependence on frequency in the Planck analysis, resulting in $T_d = 19.6 \text{ K}$ in PLA16; star in Fig. 4). The fixed power-law expression for κ_{ν}^d we adopted might not be the best choice for describing dust emission, when using a single MBB; nevertheless it proved reliable in the estimate of the dust mass (and surface density) under different heating conditions, which is important for the current analysis (see, e.g. Nersesian et al. 2019). Using the average $\epsilon_{30 \text{ GHz}}^{\text{AME}}$, we can estimate $S_{30 \text{ GHz}}^{\text{AME}}$ from $S_{3 \text{ THz}}$ and the fitted T_d (inverting Eq. 2) or from M_d (with Eq. 3): we derive $S_{30 \text{ GHz}}^{\text{AME}} \approx 5 \text{ mJy}$ (15 mJy for NGC 5055), on the lower side of the spread of Table 3 but still compatible within the large uncertainties from the fit.

In an attempt to understand what makes the detection of AME peculiar in M 31 (where $S_{30 \text{ GHz}}^{\text{AME}}$ is estimated to be about 35-70% of the total flux density, while it is a smaller fraction for the rest of the sample) we defined the radio emissivity per dust column density, $\epsilon_{1.4 \text{ GHz}}$, analogous to $\epsilon_{30 \text{ GHz}}^{\text{AME}}$ in Eq. 2 and 3 (this quantity is equivalent to divide $S_{1.4 \text{ GHz}}$ by the predicted $S_{30 \text{ GHz}}^{\text{AME}}$, if a single $\epsilon_{30 \text{ GHz}}^{\text{AME}}$ is valid for all galaxies). In Fig. 5 we plot $\epsilon_{1.4 \text{ GHz}}$ against the specific star formation rate, i.e. the star-formation rate per unit stellar mass, $sSFR = SFR/M_{\star}$, a physical quantity that shows the largest dichotomy between M 31, at the lowest value, and the rest of the sample. If we do not consider M 33, which apparently has different AME properties, $\epsilon_{1.4 \text{ GHz}}$ for M 31 is almost an order of magnitude smaller than for the other galaxies considered here. Even though more observations (and AME detections) are needed to confirm this apparent trend, one might wonder if AME could be better observed in quiescent spirals in the final stages of their evolution, such as Andromeda,

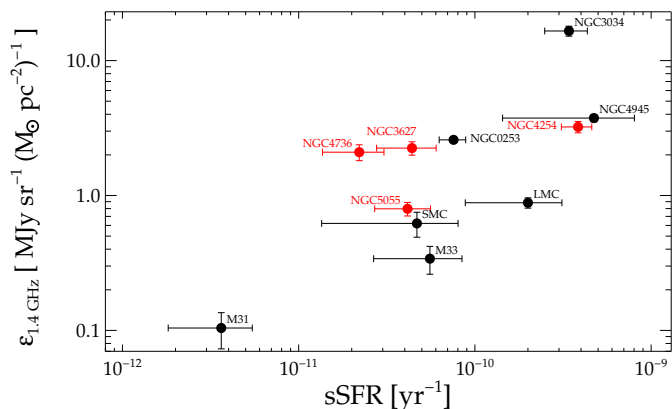


Fig. 5. $\epsilon_{1.4 \text{ GHz}}$ vs specific star formation rate, $sSFR$. Red symbols are for SRT targets. See Table A.1 for the source of $SFRs$ and M_* used to derive $sSFR$.

where the build-up of the dust mass has concluded, so that AME intensity is higher, and the radio continuum has a lower luminosity, thus allowing AME to emerge over the other SED components.

5. Conclusions

We have shown that the upper limits derived for AME in four galaxies observed at SRT (and those for three other objects in the literature) are consistent with the few AME detections, and in particular those for the MW and M 31, once a proper AME emissivity per dust surface density is defined.

The analysis presented here is only tentative, as it is based only on a few detections. Also, it implicitly relies on the main assumption that AME does not change from object to object, and that its spectrum peaks in between 20 to 30 GHz, as in the diffuse MW medium and in M 31. We already found in the small sample we analyzed one object, M 33, whose AME emissivity is substantially smaller than those for the other galaxies, possibly on account of a reduced fraction of the small grains responsible for AME (see, e.g., Calapa et al. 2014; Williams et al. 2019). Also, the spinning-grain theory predicts (and some observations in the MW suggest) that the AME spectrum peaks at higher frequency in higher density environments (see, e.g., Dickinson et al. 2018). Thus, different galaxies might have a different AME spectrum depending on the dominant ISM conditions (and on their relative proportion).

Certainly, observations of the full SED beyond 30 GHz and up to the millimeter spectral range could provide further opportunities for new detections and the characterization of AME. Furthermore, they will offer the possibility to solve the degeneracies in the continuum decomposition, without which it will not be possible to fully exploit the use of free-free radiation as a dust-free tracer of the SFR. At the SRT, high frequency observations will become possible soon with the ongoing upgrade to new Q-band (33-50 GHz) and W-band (70-116 GHz) instruments (Govoni et al. 2021).

Acknowledgements. This paper is dedicated to the memory of Jonathan I. Davies, to whom we are grateful, among many other things, for devising the DustPedia and IMEGIN projects. We thank E. S. Battistelli for useful comments and F. Radiconi for sharing with us the AME template used for the M31 analysis. SB and VC acknowledge support from the INAF main stream 2018 program ‘‘Gas-DustPedia: A definitive view of the ISM in the Local Universe’’, and from the grant PRIN MIUR 2017 - 20173ML3WW_001. The Sardinia Radio Telescope is funded by the Ministry of University and Research (MIUR), Italian Space Agency (ASI), and the Autonomous Region of Sardinia (RAS) and is

operated as National Facility by the National Institute for Astrophysics (INAF). The Enhancement of the Sardinia Radio Telescope (SRT) for the study of the Universe at high radio frequencies is financially supported by the National Operative Program (Programma Operativo Nazionale - PON) of the Italian Ministry of University and Research ‘‘Research and Innovation 2014-2020’’, Notice D.D. 424 of 28/02/2018 for the granting of funding aimed at strengthening research infrastructures, in implementation of the Action II.1 – Project Proposals PIR01_00010 and CIR01_00010.

References

- Ali-Haïmoud, Y., Hirata, C. M., & Dickinson, C. 2009, *MNRAS*, 395, 1055
 Aniano, G., Draine, B. T., Gordon, K. D., & Sandstrom, K. 2011, *PASP*, 123, 1218
 Auld, R., Bianchi, S., Smith, M. W. L., et al. 2013, *MNRAS*, 428, 1880
 Battistelli, E. S., Fatigoni, S., Murgia, M., et al. 2019, *ApJL*, 877, L31
 Bell, A. C., Onaka, T., Galliano, F., et al. 2019, *PASJ*, 71, 123
 Bianchi, S., Casasola, V., Baes, M., et al. 2019, *A&A*, 631, A102
 Bianchi, S., Murgia, M., Melis, A., et al. 2021, *Proceedings of the International Conference ‘‘mm Universe @ NIKA2’’, Rome 2021*, arXiv:2111.01428
 Braun, R., Oosterloo, T. A., Morganti, R., Klein, U., & Beck, R. 2007, *A&A*, 461, 455
 Calapa, M. D., Calzetti, D., Draine, B. T., et al. 2014, *ApJ*, 784, 130
 Clark, C. J. R., Roman-Duval, J. C., Gordon, K. D., Bot, C., & Smith, M. W. L. 2021, *ApJ*, in press [arXiv:2107.14302]
 Clark, C. J. R., Verstocken, S., Bianchi, S., et al. 2018, *A&A*, 609, A37
 Condon, J. J., Cotton, W. D., Greisen, E. W., et al. 1998, *AJ*, 115, 1693
 Corbelli, E. 2003, *MNRAS*, 342, 199
 Dale, D. A., Aniano, G., Engelbracht, C. W., et al. 2012, *ApJ*, 745, 95
 Davies, J. I., Baes, M., Bianchi, S., et al. 2017, *PASP*, 129, 044102
 de los Reyes, M. A. C. & Kennicutt, Robert C., J. 2019, *ApJ*, 872, 16
 Dickinson, C., Ali-Haïmoud, Y., Barr, A., et al. 2018, *New A Rev.*, 80, 1
 Draine, B. T. 2011, *Physics of the Interstellar and Intergalactic Medium* (Princeton University Press)
 Draine, B. T. & Lazarian, A. 1998a, *ApJ*, 494, L19
 Draine, B. T. & Lazarian, A. 1998b, *ApJ*, 508, 157
 Draine, B. T. & Lazarian, A. 1999, *ApJ*, 512, 740
 Ejlali, G., Adam, R., Ade, P., et al. 2021, in *Proceedings of the International Conference ‘‘mm Universe @ NIKA2’’, Rome 2021*, arXiv:2111.03844
 Emerson, D. T. & Graeve, R. 1988, *A&A*, 190, 353
 Fatigoni, S., Radiconi, F., Battistelli, E. S., et al. 2021, *A&A*, 651, A98
 For, B. Q., Staveley-Smith, L., Hurley-Walker, N., et al. 2018, *MNRAS*, 480, 2743
 Foreman-Mackey, D., Hogg, D. W., Lang, D., & Goodman, J. 2013, *PASP*, 125, 306
 Galliano, F., Galametz, M., & Jones, A. P. 2018, *ARA&A*, 56, 673
 Govoni, F., Bolli, P., Buffa, F., et al. 2021, in *2021 XXXIVth General Assembly and Scientific Symposium of the International Union of Radio Science (URSI GASS)*, 1–4
 Harper, S. E., Dickinson, C., & Cleary, K. 2015, *MNRAS*, 453, 3375
 Hensley, B. S. & Draine, B. T. 2021, *ApJ*, 906, 73
 Hensley, B. S., Draine, B. T., & Meisner, A. M. 2016, *ApJ*, 827, 45
 Hoang, T., Vinh, N.-A., & Quynh Lan, N. 2016, *ApJ*, 824, 18
 Jones, A. P. 2009, *A&A*, 506, 797
 Jones, A. P., Köhler, M., Ysard, N., Bocchio, M., & Verstraete, L. 2017, *A&A*, 602, A46
 Katsioli, S., Adam, R., Ade, P., et al. 2021, in *Proceedings of the International Conference ‘‘mm Universe @ NIKA2’’, Rome 2021*, arXiv:2111.01734
 Loi, F., Murgia, M., Vacca, V., et al. 2020, *MNRAS*, 498, 1628
 Melis, A., Concu, R., Trois, A., et al. 2018, *Journal of Astronomical Instrumentation*, 7, 1850004
 Murgia, M., Govoni, F., Carretti, E., et al. 2016, *MNRAS*, 461, 3516
 Murphy, E. J., Condon, J. J., Schinnerer, E., et al. 2011, *ApJ*, 737, 67
 Murphy, E. J., Helou, G., Condon, J. J., et al. 2010, *ApJ*, 709, L108
 Murphy, E. J., Linden, S. T., Dong, D., et al. 2018, *ApJ*, 862, 20
 Nashimoto, M., Hattori, M., Poidevin, F., & Génova-Santos, R. 2020, *ApJ*, 900, L40
 Nersesian, A., Xilouris, E. M., Bianchi, S., et al. 2019, *A&A*, 624, A80
 Orfei, A., Carbonaro, L., Cattani, A., et al. 2010, *IEEE Antennas and Propagation Magazine*, 52, 62
 Peel, M. W., Dickinson, C., Davies, R. D., Clements, D. L., & Beswick, R. J. 2011, *MNRAS*, 416, L99
 Perley, R. A. & Butler, B. J. 2017, *ApJS*, 230, 7
 Planck Collaboration Int. XV. 2014, *A&A*, 565, A103
 Planck Collaboration Int. XXV. 2015, *A&A*, 582, A28
 Planck Collaboration XVII. 2011, *A&A*, 536, A17
 Planck Collaboration XXV. 2016, *A&A*, 594, A25
 Prandoni, I., Murgia, M., Tarchi, A., et al. 2017, *A&A*, 608, A40
 Silsbee, K., Ali-Haïmoud, Y., & Hirata, C. M. 2011, *MNRAS*, 411, 2750
 Skibba, R. A., Engelbracht, C. W., Aniano, G., et al. 2012, *ApJ*, 761, 42
 Tabatabaei, F. S., Schinnerer, E., Krause, M., et al. 2017, *ApJ*, 836, 185
 Tibbs, C. T., Israel, F. P., Laureijs, R. J., et al. 2018, *MNRAS*, 477, 4968
 Tibbs, C. T., Paladini, R., & Dickinson, C. 2012, *Advances in Astronomy*, 2012, 124931
 Viaene, S., Baes, M., Tamm, A., et al. 2017, *A&A*, 599, A64
 Viaene, S., Fritz, J., Baes, M., et al. 2014, *A&A*, 567, A71
 Williams, T. G., Baes, M., De Looze, I., et al. 2019, *MNRAS*, 487, 2753
 Ysard, N., Juveta, M., & Verstraete, L. 2011, *A&A*, 535, A89
 Ysard, N., Miville-Deschênes, M. A., & Verstraete, L. 2010, *A&A*, 509, L1

Appendix A: Additional material

Appendix A.1: Tests on aperture photometry

Our apertures are smaller than those used to derive the flux densities in T17, which instead cover the optical size of each galaxy. For example, the 1.36 GHz flux densities listed in T17 have been obtained by Braun et al. (2007) using circular apertures of size 10 to 15', almost reaching the whole extent of the SRT maps. Since the original Westerbork Synthesis Radio Telescope images of Braun et al. (2007) are available from the NASA Extragalactic Database (NED), we used them to test the impact of our smaller apertures. We follow the procedure of Dale et al. (2012) to estimate the amount of flux that would go beyond the aperture because of beam smearing. We assume that the 1.36 GHz image can be used as a higher-resolution proxy for the surface brightness spatial distribution at the SRT frequencies, and smooth it to the SRT 18.6 GHz resolution, using Gaussian kernels. For each of our targets, the full resolution image is shown in Fig. A.1, with superimposed contours from the smoothed image. We found that the global flux densities of Braun et al. (2007) are larger than those derived by integrating the smoothed maps on our apertures, but only by a moderate factor: 3 to 5% for NGC 3627, NGC 4254 and NGC 4736. The total flux density at 1.36 GHz for NGC 5055 is instead 12% larger. However, this is due in part to point sources non related to the galaxy (some of which are visible in the southern edge of the map in Fig. A.1): when these are removed, the difference reduces to 5%. Since the errors on SRT photometry are larger, we do not apply any correction. We only note that, for NGC 5055, the additional flux density picked from the background sources might affect also the other large-aperture flux densities quoted by T17. Thus, before SED fitting, one should lower those flux densities down by about 7%. Even if this slightly changes the values of the fitted parameters, it has little effect on the general results for this galaxy. Thus, we do not implement this correction either.

In this work we also made use of DustPedia 3 THz flux densities, obtained by integrating *Herschel* 100 μm images over apertures matched to contain all emission from the UV to the submm (Clark et al. 2018). We repeated the same exercise on the images from the DustPedia archive: the full resolution maps are shown in the bottom panel of Fig. A.1, with superimposed contours from the same maps smoothed to the SRT resolution (using the convolution kernels of Aniano et al. 2011). This time the flux densities obtained over the larger aperture are almost the same, for NGC 3627 and NGC 4736. For NGC 4254 and NGC 5055, instead, the DustPedia flux densities are *smaller* than those derived on the apertures defined here. Nevertheless, the difference is still compatible with the photometric uncertainties, highlighting the fact that apertures much larger than the apparent size of the objects, though functional in detecting all of the emission, can also result in larger uncertainties, due to fluctuations in the sky background and unremoved sources other than the one of interest.

Appendix A.2: Details on SED fitting

In Fig. A.2 we show the Bayesian corner plots for the parameters derived from the fit. The figure also shows the marginalized PDF for each parameter together with the median and 0.16 and 0.84 percentiles.

Appendix A.3: Ancillary data

Table A.1 lists the quantities used for producing Fig. 4 and Fig. 5. Beside the upper limits for $S_{24.6\text{ GHz}}^{\text{AME}}/S_{3\text{ THz}}$ for our galaxy sample, and the single-T MBB fits to the reference targets done in this work, all other data are culled from the literature.

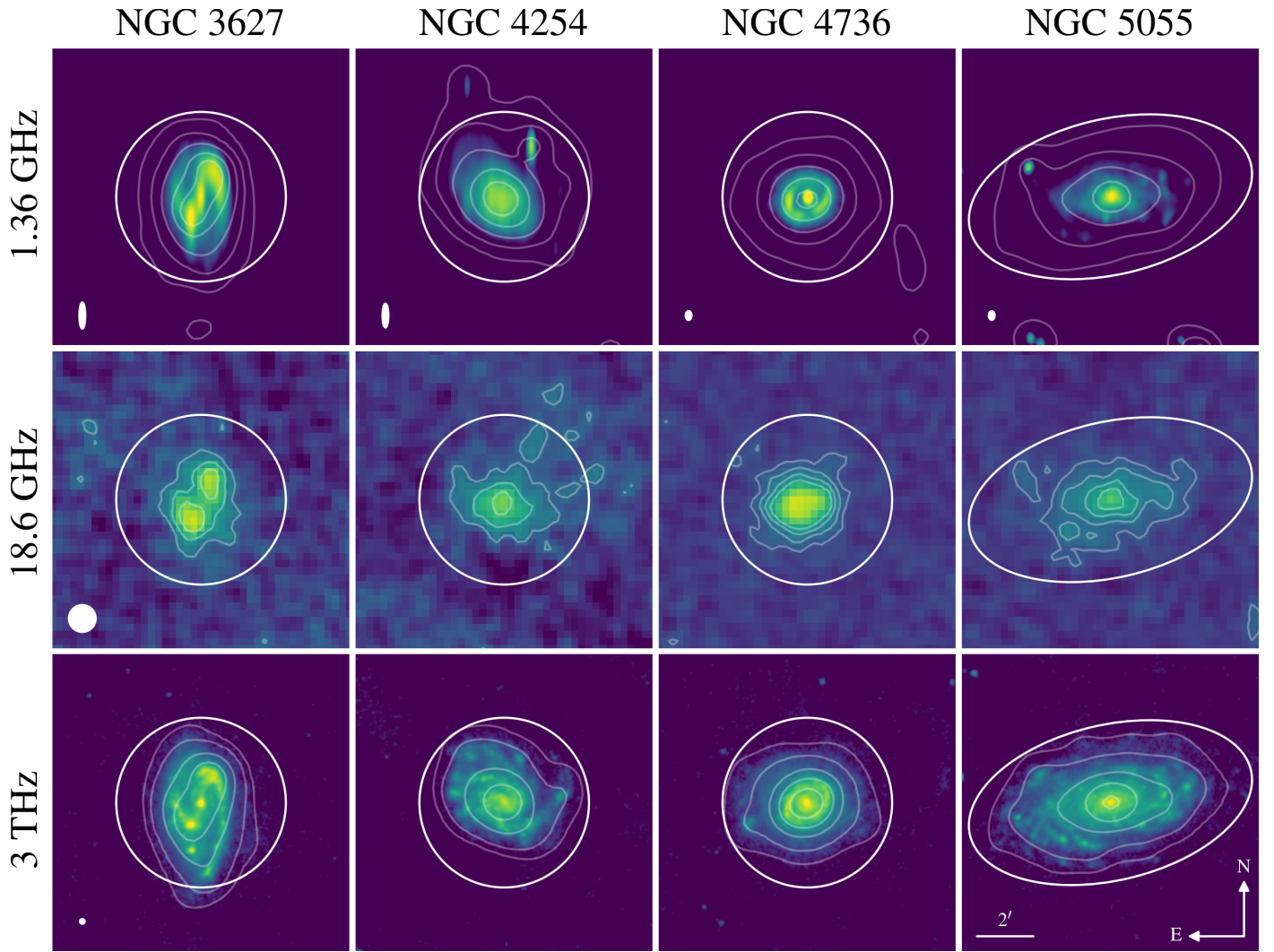


Fig. A.1. Top panels: Westerbork Synthesis Radio Telescope images from Braun et al. (2007); the white ellipses show the synthesized beams; the contours show the same maps smoothed to the SRT 18.6 GHz resolution (HPBW=57''), at surface brightness levels of 0.025, 0.1, 0.25, 0.5, 0.75 MJy sr⁻¹. Bottom panels: *Herschel* 3 THz (100 μ m) maps from DustPedia, with HPBW=10'' (white circle); the contours show the maps smoothed to the SRT resolution, at 5, 20, 100, 250, 500 MJy sr⁻¹. As a reference, the SRT images at 18.6 GHz are shown in the central panel (same as in Fig. 1). The apertures adopted in our work are also shown.

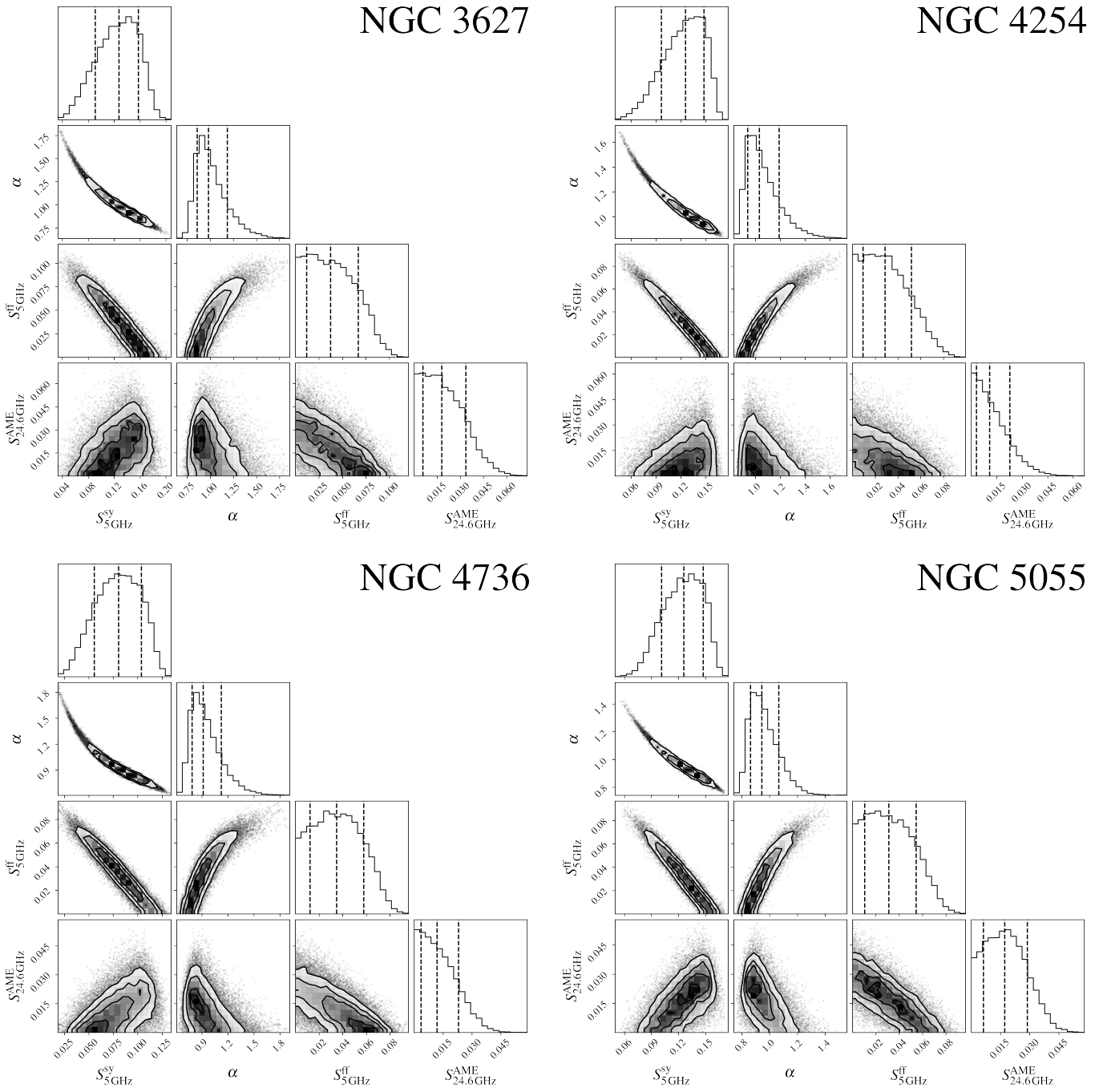


Fig. A.2. Corner plots for the parameters describing the SED. Flux densities are in Jy. Marginalized PDFs are shown, the dashed lines marking median values and 0.16 and 0.84 percentiles.

Table A.1. Data of Fig. 4 and Fig. 5.

names	distance ^a Mpc	$S_v^{\text{AME}}/S_{3\text{THz}}$	$S_{1.4\text{GHz}}$ Jy	T_d K	M_d M_\odot	M_\star M_\odot	SFR $M_\odot \text{ yr}^{-1}$
NGC 3627	11.5	$< 2.3 \times 10^{-4}$ ^c	0.50 ± 0.01^h	25.3 ± 0.8^m	$2.9 \pm 0.3 \times 10^7$	$6.7 \pm 1.2 \times 10^{10}$	2.9 ± 1.0
NGC 4254	12.9	$< 3.1 \times 10^{-4}$ ^c	0.51 ± 0.02^h	24.3 ± 0.8^m	$2.6 \pm 0.2 \times 10^7$	$1.3 \pm 0.2 \times 10^{10}$	5.1 ± 0.5
NGC 4736	4.4	$< 1.8 \times 10^{-4}$ ^c	0.295 ± 0.005^h	26 ± 1^m	$2.7 \pm 0.4 \times 10^6$	$2.5 \pm 0.4 \times 10^{10}$	0.55 ± 0.19
NGC 5055	9.0	$< 2.2 \times 10^{-4}$ ^c	0.460 ± 0.005^h	21.3 ± 0.7^m	$4.7 \pm 0.5 \times 10^7$	$5.9 \pm 1.1 \times 10^{10}$	2.5 ± 0.7
MW	-	$3.4 \pm 0.3 \times 10^{-4}$ ^d	-	18.3 ± 0.3^n	-	-	-
LMC	0.05^b	$1.4 \pm 0.2 \times 10^{-4}$ ^d	530 ± 30^i	21.1 ± 0.4^o	$1.5 \pm 0.1 \times 10^6$	$2.0 \pm 0.5 \times 10^9$ ^q	0.4 ± 0.2
SMC	0.062^b	$7.5 \pm 2.4 \times 10^{-5}$ ^d	42 ± 6^i	20.2 ± 0.8^o	$2.6 \pm 0.4 \times 10^5$	$3.2 \pm 0.8 \times 10^9$ ^q	0.015 ± 0.010
M 31	0.79^b	$4.2 \pm 0.6 \times 10^{-4}$ ^e	5.2 ± 0.4^j	17.3 ± 0.1^o	$3.1 \pm 0.1 \times 10^7$	$5.5 \pm 0.1 \times 10^{10}$ ^r	0.2 ± 0.1^s
M 33	0.04^b	$< 3.5 \times 10^{-5}$ ^f	2.7 ± 0.6^k	18.9 ± 0.3^o	$5.6 \pm 0.4 \times 10^6$	$4.5 \pm 1.5 \times 10^9$ ^t	0.25 ± 0.10^u
NGC 253	3.7	$< 3.1 \times 10^{-5}$ ^g	6.2 ± 0.1^l	26.2 ± 0.2^p	$3.3 \pm 0.1 \times 10^7$	$7.6 \pm 0.8 \times 10^{10}$ ^v	5.8 ± 0.8
NGC 3034	3.6	$< 4.0 \times 10^{-5}$ ^g	8.4 ± 0.3^l	35 ± 1^p	$6.6 \pm 0.5 \times 10^6$	$1.3 \pm 0.3 \times 10^{10}$ ^w	4.5 ± 0.6
NGC 4945	3.5	$< 4.2 \times 10^{-5}$ ^g	6.4 ± 0.2^l	26.4 ± 0.4^m	$2.1 \pm 0.3 \times 10^7$	$1.4 \pm 0.6 \times 10^{10}$	6.5 ± 3.6

Notes. ^(a) Unless otherwise specified, distances are from the DustPedia database, available at <http://dustpedia.astro.noa.gr/>. ^(b) From Clark et al. (2021). ^(c) From this work and the *Herschel* $S_{3\text{THz}}$ in DustPedia. ^(d) Estimated at 22.8 GHz in PLA16. ^(e) Estimated at 30 GHz in Battistelli et al. (2019). ^(f) From the upper limit of Tibbs et al. (2018) at 30 GHz and $S_{3\text{THz}}$ in Clark et al. (2021). ^(g) From the upper limit of P11 between 23 and ≈ 100 GHz and *Herschel* $S_{3\text{THz}}$ in DustPedia, with the exception of NGC 3034, for which $S_{3\text{THz}}$ was estimated from the SED fit. ^(h) T17; for NGC 3627 we used $S_{1.36\text{GHz}}$. ⁽ⁱ⁾ For et al. (2018). ^(j) Battistelli et al. (2019). ^(k) Tibbs et al. (2018). ^(l) P11. ^(m) T_d and M_d from FIR-submm MBB fits, M_\star and SFR from optical-to-submm fits (Nersesian et al. 2019). ⁽ⁿ⁾ This work; MBB fits of the MW diffuse dust emissivity for $100 \leq \lambda/\mu\text{m} \leq 850$ from Hensley & Draine (2021). ^(o) This work; T_d and M_d from MBB fits of *Herschel* flux densities from Clark et al. (2021). ^(p) This work; T_d and M_d from MBB fits of *Herschel* flux densities in DustPedia. ^(q) M_\star and SFR from Skibba et al. (2012). ^(r) Viaene et al. (2014). ^(s) Viaene et al. (2017). ^(t) Corbelli (2003). ^(u) Williams et al. (2019). ^(v) M_\star and SFR from de los Reyes & Kennicutt (2019). ^(w) M_\star and SFR from Nersesian et al. (2019).